Journal of
Composites Science

MDPI

Article

Tailoring Fe-Pt Composite Nanostructures Through Iron Precursor Selection in Aqueous Low-Temperature Synthesis

Anna N. Prigorodova [1,*], Nikita S. Zakharov [1], Valery M. Pugachev [1], Alexander N. Shmakov [2], Nickolay S. Adodin [1] and Dmitry M. Russakov [1]

[1] Federal Research Center of Coal and Coal Chemistry SB RAS, Kemerovo 650099, Russia
[2] Resource Sharing Center "The Siberian Circular Photon Source", Koltsovo 630559, Russia
* Correspondence: h991@yandex.ru; Tel.: +7-923-489-9454

Abstract

This study addresses the challenge of low-temperature synthesis of the high-performance $L1_0$ Fe-Pt intermetallic phase, which is critical for applications in ultra-high-density data storage and advanced magnetic devices. We demonstrate that the choice of iron precursor is a decisive factor in directing the phase composition and thermal evolution of Fe-Pt nanostructures, ultimately determining their suitability as functional composite materials. Fe-Pt systems were synthesized from aqueous solutions using platinum(IV) chloric acid (H_2PtCl_6) with either iron(III) ammonium sulfate ($NH_4Fe(SO_4)_2$) or iron(II) sulfate ($FeSO_4$). Comprehensive characterization using X-ray diffraction and high-resolution transmission electron microscopy revealed distinct composite formations. The iron(III) precursor yielded homogeneous, thermally stable nanocomposites: as-synthesized nanoparticles formed a Pt-based FCC solid solution (~5 nm), which upon annealing at 500 °C transformed into a biphasic nanocomposite of FCC solid solution and an $L1_2$ $Fe_{21}Pt_{79}$ intermetallic phase with minimal grain growth (~7 nm). In stark contrast, the system derived from iron(II) sulfate resulted in a heterogeneous composite of 4 nm Pt nanoparticles, an FCC solid solution, and discrete 1–3 nm Fe nanoparticles with $L1_2$-ordered $FePt_3$ domains. Annealing this heterogeneous mixture caused phase segregation, forming significantly coarsened Pt-rich crystals (~30 nm) that were approximately 4–6 times larger than the crystallites in the annealed homogeneous composite, with negligible Fe incorporation. Our findings establish that precursor chemistry dictates the initial nanocomposite architecture, which in turn controls the pathway and success of low-temperature intermetallic phase formation. This work provides a crucial design principle for fabricating tailored Fe-Pt composite nanomaterials, moving beyond simple alloys to engineered multiphase systems for practical application.

Keywords: Fe-Pt nanocomposites; iron precursor; low-temperature synthesis; phase evolution; biphasic materials; $L1_2$ intermetallic phase; structural characterization

check for updates

Academic Editor: Prashanth Konda Gokuldoss

Received: 30 September 2025
Revised: 30 October 2025
Accepted: 2 November 2025
Published: 8 November 2025

Citation: Prigorodova, A.N.; Zakharov, N.S.; Pugachev, V.M.; Shmakov, A.N.; Adodin, N.S.; Russakov, D.M. Tailoring Fe-Pt Composite Nanostructures Through Iron Precursor Selection in Aqueous Low-Temperature Synthesis. *J. Compos. Sci.* **2025**, *9*, 616. https://doi.org/10.3390/jcs9110616

Copyright: © 2025 by the authors. Licensee MDPI, Basel, Switzerland. This article is an open access article distributed under the terms and conditions of the Creative Commons Attribution (CC BY) license (https://creativecommons.org/licenses/by/4.0/).

1. Introduction

The pursuit of advanced magnetic materials for ultra-high-density data storage, permanent magnets, and nanomedicine drives the need for nanostructured systems with exceptional coercivity and saturation magnetization, retained under demanding operational conditions [1–3]. Among the most promising candidates are nanocomposites based on the Fe-Pt system, particularly the $L1_0$-FePt intermetallic phase, which combines an

ultrahigh coercive force (up to 116 kOe) with high chemical stability and significant saturation magnetization [1,4–9]. This unique property profile makes Fe-Pt composites ideal for applications ranging from accelerator components (wigglers, deflection magnets) to targeted drug delivery and catalysis [10–16].

A central challenge in realizing the full theoretical potential of these materials—currently estimated at less than 50% achievement—lies in the synthesis of well-defined, homogeneous precursors for subsequent thermal processing [1,17–19]. The desired $L1_0$ phase typically requires high-temperature annealing of a disordered face-centered cubic (FCC) solid solution. However, the synthesis of this initial FCC phase is often complicated by the disparate reduction potentials of iron and platinum precursors. The faster reduction kinetics of platinum typically lead to heterogeneous systems comprising Pt-rich nanoparticles and separate Fe phases, rather than a homogeneous solid solution [9,17,20,21]. Upon annealing, such heterogeneity promotes undesirable phase segregation and coarse grain growth, ultimately impeding the formation of the desired fine-grained, homogeneous intermetallic composite [9,20,21].

While co-reduction in alkaline hydrazine hydrate (N_2H_4*H_2O) offers a practical and scalable aqueous route [22], it often yields a mixture of phases [23], including high-Pt FCC solid solutions and various intermetallics [18]. The resulting multiphase architecture is suboptimal for achieving a controlled transformation into a high-performance material.

Therefore, this study addresses the critical need to control the initial composite nanostructure by investigating the influence of iron precursor chemistry. We hypothesize that the choice of precursor—specifically, the oxidation state and associated counterions—can modulate reduction kinetics and direct the pathway of phase formation. By using iron(III) ammonium sulfate and iron(II) sulfate with chloroplatinic acid, we aim to engineer the initial nanocomposite architecture to favor the development of a homogeneous, thermally stable Fe-Pt material. The goal is to establish a synthesis-property relationship that provides a fundamental design principle for fabricating tailored metal composites via a low-temperature aqueous route, thereby advancing their practical application.

2. Materials and Methods

2.1. Aqueous Synthesis of Fe-Pt Nanocomposites

Fe-Pt nanostructured systems were synthesized via a co-reduction method in an aqueous medium, designed to investigate the influence of iron precursor chemistry on the resulting composite's phase composition and homogeneity. The synthesis was performed in a closed chemical reactor (Zhongyi Kori Equipment SF-1L, Zhongyi Kori Equipment, Shanghai, China) under a continuous high-purity argon atmosphere to prevent oxidation. The temperature was maintained at 90 °C using a circulation thermostat (LOIP LT-124a, LOIP Ltd., St. Petersburg, Russia).

To engineer distinct composite architectures, two different iron precursors were employed:

- system A (Fe(III)-based): iron(III) ammonium sulfate ($NH_4Fe(SO_4)_2$) in a dilute HNO_3 supporting electrolyte;
- system B (Fe(II)-based): iron(II) sulfate ($FeSO_4$) in a dilute H_2SO_4 supporting electrolyte.

For both systems, platinum was introduced from a chloroplatinic acid (H_2PtCl_6) solution in a dilute HCl supporting electrolyte. The molar ratio of Fe:Pt was fixed at 15:85 for all syntheses. The choice of precursors was strategic; the different oxidation states (Fe^{3+} vs. Fe^{2+}) and counterions were expected to modulate the reduction kinetics relative to the Pt^{4+} precursor, thereby influencing the homogeneity of the resulting metal composite.

An excess of a preheated (80 °C) alkaline hydrazine hydrate ($N_2H_4 \cdot H_2O$) solution was rapidly introduced into the stirred precursor mixture (approx. 5× *g* for 10 min) to initiate co-reduction. The reaction proceeded for 5 min, yielding a suspension of metal nanoparticles.

The resulting nanocomposite powders were isolated by centrifugation (~1400× *g* for 10 min, Laboratory Centrifuge Liston C2202, Liston, Novosibirsk, Russia) and sequentially washed with deionized water (until neutral pH) and isopropyl alcohol to remove ionic byproducts and residual water. Final drying was conducted under vacuum (residual pressure $\leq$ 5 mm Hg) at room temperature until a constant weight was achieved. The key synthesis parameters for each composite are summarized in Table 1.

Table 1. Sample synthesis conditions.

Composite No.	Target Fe/Pt Ratio *	Platinum Precursor/ Supporting Electrolyte **	Iron Precursor/ Supporting Electrolyte **
1	15/85	$H_2[PtCl_6]$/HCl	$FeSO_4/H_2SO_4$
2	15/85	$H_2[PtCl_6]$/HCl	$NH_4Fe(SO_4)_2/HNO_3$

*—Here and thereafter, the composition of metal phases is expressed as at.%. **—Supporting electrolytes are necessary to prevent the hydrolysis reaction resulting in poorly soluble compounds.

2.2. Elemental Analysis of Composite Powders

The overall elemental composition of the synthesized Fe-Pt nanocomposite powders was determined by inductively coupled plasma–optical emission spectrometry (ICP–OES) to verify the target Fe:Pt molar ratio and assess purity. This analysis was crucial for confirming the successful co-reduction of both metal precursors and the absence of significant contamination, which could influence the phase behavior and properties of the final composite material.

An analytical sample of the dry powder was completely digested in a mixture of concentrated nitric and hydrochloric acids. The resulting solution was analyzed using an iCAP 6500 Duo spectrometer (Thermo Electron Corporation, Waltham, MA, USA) operating in radial plasma observation mode at a power of 1150 W. The concentrations of the main components (Fe, Pt) and potential impurities were determined at characteristic wavelengths selected to be free of spectral interference. Reported values represent the average of concentrations measured at different analytical wavelengths for each element, ensuring accuracy.

The ICP-OES results were compared with Fe/Pt ratios determined by energy-dispersive X-ray (EDX) spectroscopy. EDX analysis was performed using a JEOL JED-2300 spectrometer (JEOL Ltd., Tokyo, Japan) attached to a scanning electron microscope, operating at 20 kV with a magnification of 10,000×.

2.3. Structural Characterization of Composite Phases and Thermal Stability

The phase composition, crystal structure, and thermal evolution of the synthesized Fe-Pt nanocomposites were investigated using a combination of X-ray diffraction and high-resolution electron microscopy.

2.3.1. X-Ray Diffraction (XRD) Analysis

XRD analysis was performed to identify the crystalline phases present in the as-synthesized and annealed composites. Data were collected using two sources:

1. laboratory XRD: a Bruker D8 ADVANCE A25 diffractometer (Bruker AXS GmbH, Karlsruhe, Germany) with Cu Kα radiation (Ni filter) was used, scanning from 10–90° 2θ with a step size of 0.02°;
2. synchrotron radiation (SR) XRD: High-resolution patterns were acquired at the VEPP-4M storage ring (λ = 0.17836 Å) in transmission mode using a MAR3450 detector

(Marresearch GmbH, Hamburg, Germany) (2θ range: 1–25°) [24]. Two-dimensional patterns were integrated into one-dimensional intensity profiles [25].

Phase identification was conducted using DIFFRAC.EVA V4.2 software with the ICDD PDF-2 [26] and Crystallography Open Database (COD). Instrumental broadening was calibrated using a LaB_6 standard (NIST SRM 660b). The estimated experimental error is ±0.00X Å, which corresponds to an uncertainty in composition of approximately 0.5%.

2.3.2. In-Situ High-Temperature XRD for Phase Evolution

To study the thermal stability and phase transformations of the composites, powder samples were heated from 30 to 500 °C (holding time: 3 h) under high vacuum (10^{-7} mbar) using an Anton Paar HTK 1200N oven chamber (Anton Anton Paar GmbH, Graz, Austria). A slow heating rate of 1 °C/min was employed to monitor phase evolution effectively. Prior to heating, the chamber was degassed at 80 °C for 1.5 h to minimize sample oxidation.

All XRD patterns were processed, and structural parameters—including phase composition and coherent scattering region (CSR) sizes—were refined using the GSAS-II (V5.6.0) software package [27] based on established procedures [19,28].

2.3.3. High-Resolution Transmission Electron Microscopy (HRTEM)

The nanoscale morphology, particle size, and local crystal structure of the composites were examined by HRTEM using a JEOL JEM 2100 microscope (JEOL Ltd., Tokyo, Japan). Bright-field imaging was used to assess particle homogeneity and dispersion. Lattice fringe analysis was performed using ImageJ (V1.53e) software [29], and crystallographic identification was supported by the ICDD PDF-2 database [26] and VESTA (V3.5.8) software [30].

2.4. Theoretical Analysis of Phase Stability

To complement the experimental findings, the theoretical stability of solid phases under the synthesis conditions (pH~13, E~–1.1 V, C(Fe) = 1.13×10^{-3} mol/L, C(Pt) = 6.4×10^{-3} mol/L) was estimated by constructing a Pourbaix diagram using density functional theory (DFT) data from The Materials Project, following the methodology outlined in [31].

3. Results

3.1. Elemental Composition and Theoretical Phase Stability of Fe-Pt Composite Powders

Elemental analysis by ICP-OES confirmed that the synthesized powders matched the nominal composition, consistently achieving the target Fe:Pt molar ratio of 15:85. Furthermore, trace impurities of Ni, Cu, Zn, and Si were identified, with a cumulative concentration not exceeding 0.2 wt.%. All subsequent compositional data, unless otherwise noted, were determined by ICP-OES.

This verifies the quantitative co-reduction of both metal precursors and the successful formation of a solid phase with the intended overall composition, a crucial first step in fabricating the desired Fe-Pt composite. However, the overall stoichiometry does not guarantee a homogeneous distribution of elements at the nanoscale—a critical factor defining the composite's properties—was found to be highly dependent on the iron precursor used.

To gain insight into the thermodynamic driving forces during synthesis, a Pourbaix diagram was constructed for conditions approximating the experimental environment (pH~13, reduction potential E~−1.1 V) (Figure 1). The calculations predict the stability of two distinct phases: a pure platinum phase and a Fe-Pt intermetallic phase containing approximately 25 at.% iron. This phase separation is thermodynamically favored due to the significantly faster reduction kinetics of the platinum precursor ($[PtCl_6]^{2-}$) compared to the iron precursors, a consequence of their differing redox potentials.

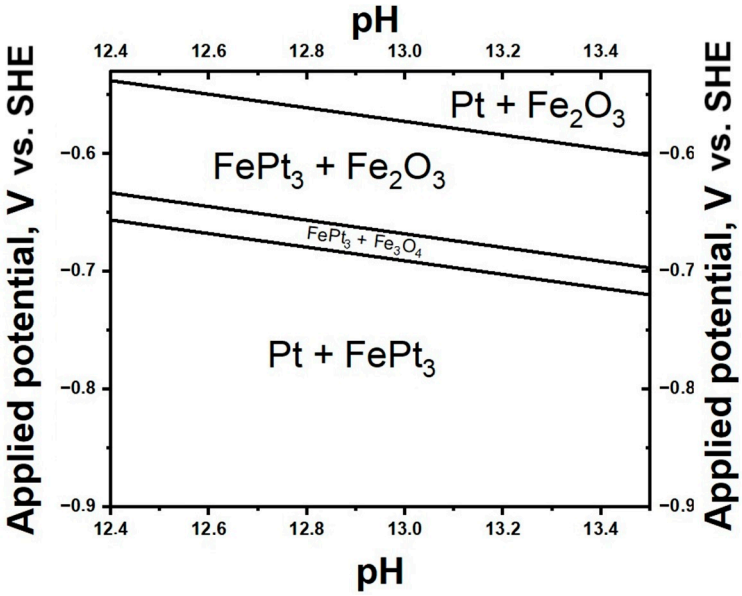


Figure 1. Pourbaix diagram.

This theoretical prediction underscores a fundamental challenge in the aqueous synthesis of homogeneous Fe-Pt nanocomposites: the inherent tendency for phase segregation. The following sections present our key finding—that the choice of iron precursor provides a critical kinetic handle to overcome this tendency and direct the formation of either a heterogeneous mixture or a more homogeneous nanocomposite architecture.

3.2. X-Ray Diffraction Analysis, HRTEM and SAED: Revealing Precursor-Dependent Composite Architecture and the Full Composite Morphology

XRD analysis of the as-synthesized samples confirms the formation of Fe-Pt nanocomposites based on a face-centered cubic (FCC) solid solution structure (Figure 2). The detection of a low-intensity FeO reflection in both samples further indicates a minor oxide component within the composite mixture. However, the diffraction patterns reveal stark differences in phase homogeneity directly attributable to the iron precursor used, defining two distinct types of composite architectures.

For the samples synthesized from the iron(II) sulfate precursor (Composite 1), the diffraction pattern is characterized by an asymmetric reflection profile (Figure 3a), indicating the presence of at least two distinct crystalline phases with different iron contents. This peak asymmetry is a clear signature of a heterogeneous nanocomposite system.

Profile fitting analysis quantitatively deconvolutes this structure into two primary FCC phases:

1. a Pt-rich FCC solid solution (as a dominant phase, ~61% of the crystalline fraction) with a lattice parameter of 3.923 Å, consistent with nearly pure platinum, and a small crystallite size of ~4 nm;
2. an Fe-Pt FCC solid solution with a smaller lattice parameter of 3.903 ± 0.001 Å, corresponding to an iron content of 9.8 at.% and larger crystallites of ~10 nm.

This phase separation is driven by the faster reduction kinetics of platinum relative to Fe^{2+} [17], leading to the initial formation of Pt-rich nuclei and supporting the hypothesis of a concomitant, ultra-dispersed iron-rich phase that is X-ray amorphous—previously termed the X-ray non-detectable phase (XRNDPh) [17,18].

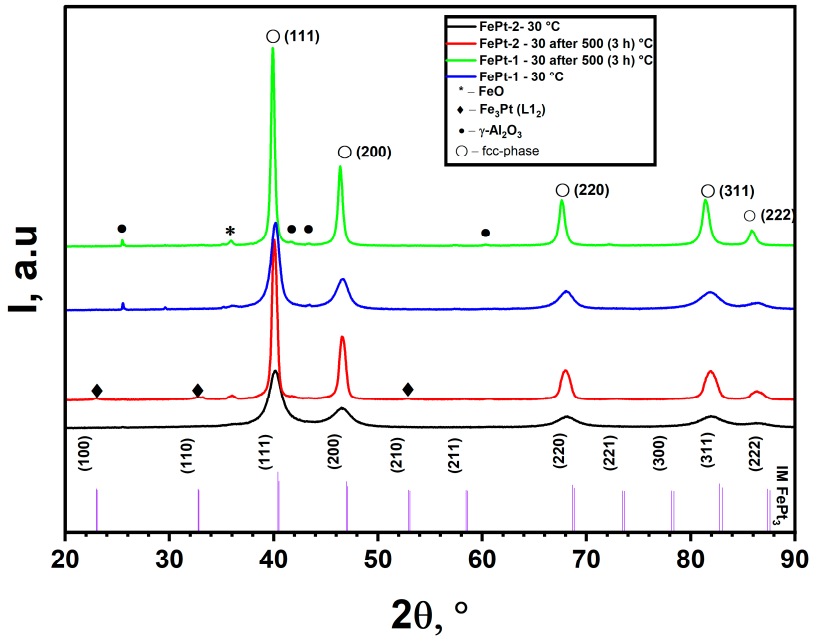
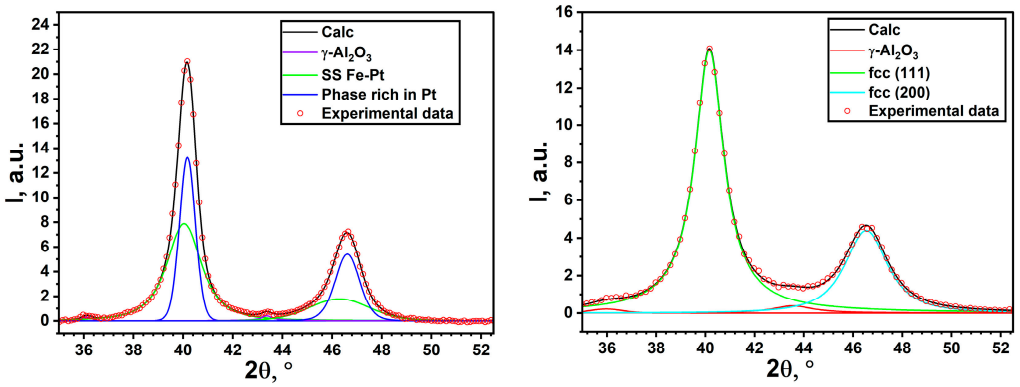


Figure 2. X-ray diffraction patterns of samples ($\lambda_{Cu,K\alpha}$ = 1.5418 Å) (peaks marked with a bullet (•) originate from the α-Al_2O_3 sample holder).



(**a**) (**b**)

Figure 3. (**a**) Fitting of (111) and (200) reflections of the FCC phase in Composite 1 with two Pearson VII functions; (**b**) Fitting of (111) and (200) reflections of the FCC phase in Composite 2 with two Pearson VII functions with allowance for the X-ray doublet reflection ($\lambda_{Cu,K\alpha}$ = 1.5418 Å).

High-resolution TEM imaging also provides direct evidence of the heterogeneity, revealing a nanostructured composite comprising several distinct phases (Figure 4):

1. ultra-fine metallic iron (XRNDPh): particles of 1–3 nm identifiable as pure FCC iron (PDF No. 88-2324) with lattice fringes (2.41 Å, 1.99 Å), which correspond to the (110) and (111) planes [25];
2. $FePt_3$ intermetallic domains: these iron particles are often adjacent to larger (8–10 nm) particles exhibiting lattice spacings of 2.72 Å, which correspond to the (110) planes of the $L1_2$-ordered $FePt_3$ intermetallic phase (PDF № 01-071-8366) [25];
3. Fe-Pt solid solutions: particles with intermediate lattice spacings (2.27 Å, 2.10 Å) confirm the presence of FCC solid solutions with varying iron content (~10 at.% to ~50 at.% Fe).

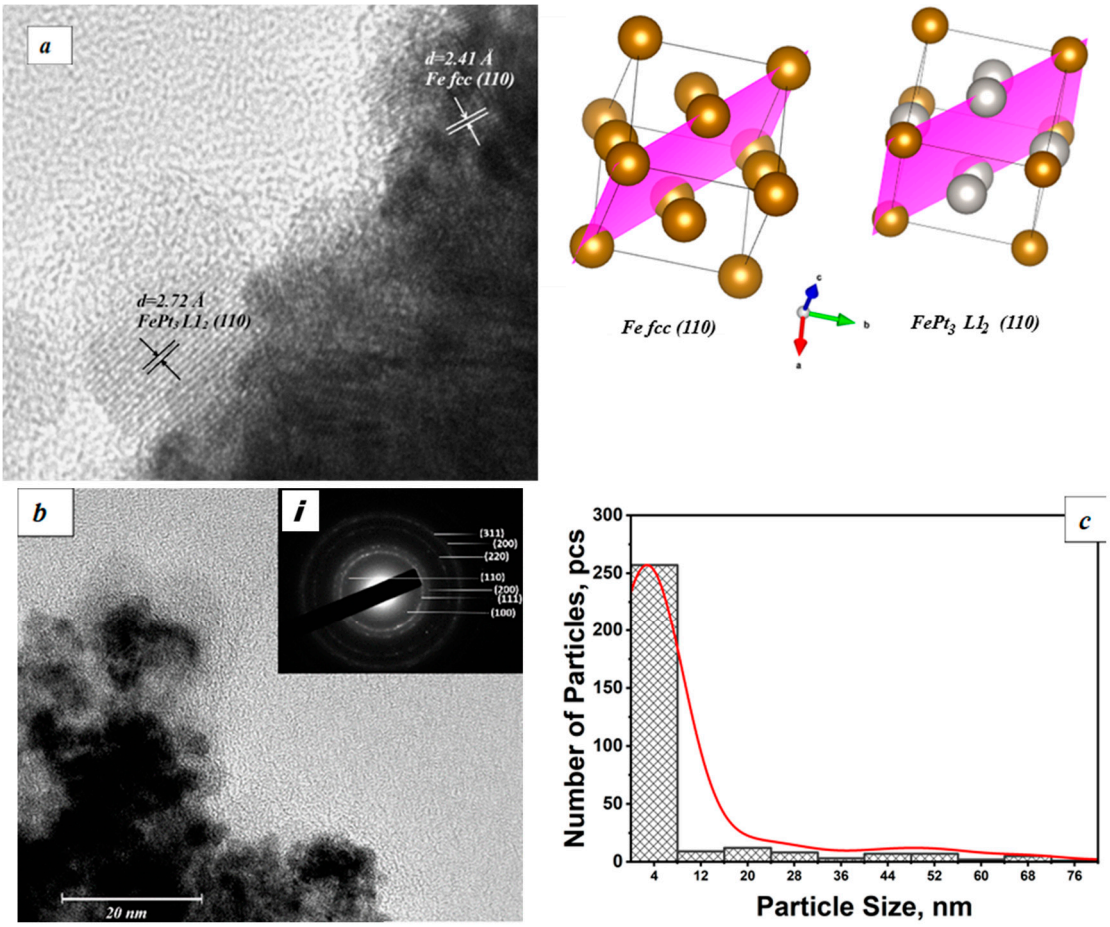


Figure 4. (**a**,**b**) TEM images of Composite 1 (schematic models of the structures: the different colors of the balls correspond to Fe (iron, brown) and Pt (platinum, grey) atoms); insert (i) SAED; (**c**) Particle size distribution in Composite 1 (according to TEM).

The presence of the $FePt_3$ ($L1_2$) intermetallic phase, albeit in low fraction, is further confirmed by Selected-Area Electron Diffraction (SAED), which shows weak but identifiable superstructure reflections (Figure 4b, Insert i).

In stark contrast to Composite 1, the composite synthesized from the iron(III) ammonium sulfate precursor (Composite 2) exhibits a markedly different and more uniform structure. The XRD pattern is characterized by symmetrical diffraction reflections that are well-fitted by a single Pearson VII function (Figure 3b). This indicates the formation of a highly homogeneous nanocomposite, primarily consisting of a single-phase FCC solid solution.

The lattice parameter of this phase is 3.897 Å, corresponding to a solid solution with 12.6 at.% iron. This value is notably close to the target stoichiometry of 15 at.% Fe, demonstrating a highly effective and near-homogeneous co-reduction process. The small, uniform crystallite size of ~5 nm—half that of the primary Fe-Pt phase in Composite 1—further underscores the uniformity of this composite precursor. The minor discrepancy between the target and measured iron content suggests that a small fraction of iron (~2%) may reside in ultra-dispersed amorphous clusters (XRNDPh), but this does not detract from the primary finding of a dominant, well-mixed solid solution.

This structural homogeneity is a direct consequence of the iron(III) precursor chemistry, which moderates the reduction kinetics to favor the concurrent incorporation of both metals into a single-phase matrix. The result is a superior nanocomposite precursor, engineered for a more controlled and predictable transformation upon subsequent thermal processing.

Thermal treatment of the two composites at 500 °C induces dramatically different transformation pathways in the two composites. This divergence underscores that the initial nanocomposite structure is critical for phase stability and microstructural evolution, thereby separating the heterogeneous system from the high-performance composite.

Upon annealing, the heterogeneous architecture of Composite 1 (from Fe(II) sulfate) proves to be highly unstable. Instead of forming beneficial intermetallic phases, it undergoes severe phase segregation and coarsening. This results in the formation of large, ~30 nm Pt-rich nanocrystals with a lattice parameter of 3.922 Å, containing a negligible 1 at.% iron.

This deleterious transformation is driven by the synergistic effect of two factors inherent to the initial heterogeneous composition. Firstly, interfacial energy-driven segregation provides the initial driving force, as the large interface area between the distinct Pt-rich and Fe-rich domains causes iron to diffuse out of the Pt lattice. Secondly, this segregation is then locked in and accelerated by the oxidation of metastable phases. The high fraction of finely dispersed, high-surface-energy iron (XRNDPh) is highly susceptible to oxidation by residual oxygen, which effectively removes iron from the alloying process and further promotes the growth of Pt-dominated crystals.

The result is a failed transformation, yielding a coarse, Pt-rich material with poor composite integrity devoid of the intended magnetic properties.

In stark contrast, the homogeneous nanocomposite from iron(III) ammonium sulfate (Composite 2) undergoes a controlled and desirable phase evolution under identical annealing conditions. The resulting material is a stable, biphasic nanocomposite evidenced by three key features: the emergence of clear superstructure reflections confirms the formation of a 65% fraction of the $L1_2$-ordered $FePt_3$ intermetallic phase; this intermetallic coexists with an FCC solid solution that retains its iron content (13.3 at.%); and the system successfully suppresses grain growth, maintaining a fine crystallite size of just ~7 nm.

The intermetallic phase combines with the FCC solid solution to create a complex and stable composite architecture.

4. Discussion

The combined XRD and HRTEM/SAED data unequivocally show that Composite 1 is a highly heterogeneous nanocomposite. It consists of a mixture of Pt-rich nanocrystals, an Fe-Pt solid solution, discrete metallic iron nanoparticles, and localized domains of the $FePt_3$ intermetallic phase. This complex morphology results from the pronounced disparity in reduction kinetics when using the Fe(II) precursor, leading to a non-uniform architecture that is likely to evolve unfavorably upon thermal treatment.

The key conclusion from the XRD analysis is that the iron(III) precursor promotes a more homogeneous distribution of iron within the platinum matrix at the earliest stages of formation, leading to a finer and more uniform nanocomposite precursor. In contrast, the iron(II) system exhibits a stronger tendency for phase separation, resulting in a more heterogeneous composite architecture. This fundamental difference in initial structure is critical for determining the thermal evolution pathway of these materials.

The divergent behavior of the two composites establishes a fundamental design principle: the initial homogeneity of the composite precursor dictates its thermal stability and phase evolution. The homogeneous architecture of Composite 2 facilitates a solid-state reaction leading to a refined, biphasic intermetallic nanocomposite. In contrast, the inherent heterogeneity of Composite 1 triggers phase separation and coarsening, destroying the composite's nanoscale features and functional potential.

The structural models derived from laboratory XRD are conclusively verified by high-resolution synchrotron radiation (SR) data (Figure 5). The high intensity and resolution of

the SR beam allow for a more precise analysis of the diffraction patterns, particularly in the high-angle region.

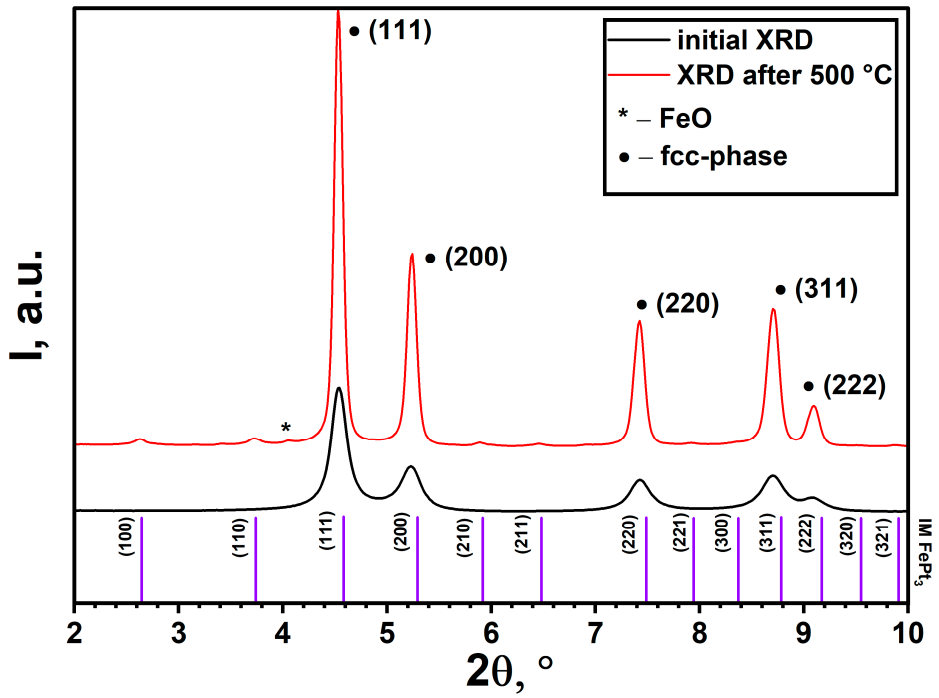


Figure 5. X-ray diffraction patterns of a FePt sample (performed on synchrotron radiation, λ = 0.17836 Å).

The enhanced data quality is crucial for elucidating the composite structure, primarily by confirming the phase identification for both samples and thereby solidifying the distinction between the homogeneous solid solution (Composite 2) and the multi-phase system (Composite 1). Furthermore, the extended range of measurable scattering vectors permits a more robust construction of the atomic Pair Distribution Function (PDF).

The planned PDF analysis will resolve the local atomic structure, enabling us to quantify short-range order and definitively characterize the X-ray non-detectable phase (XRNDPh). This will establish the atomic-scale foundation for the composite's macroscopic thermal stability and magnetic performance.

The superior signal-to-noise ratio and peak resolution offer unambiguous evidence for the homogeneous solid solution in the Fe(III)-derived composite (Composite 2) and the complex, multi-phase mixture in the Fe(II)-derived composite (Composite 1), firmly linking precursor chemistry to nanoscale composite structure.

The distinct structural and phase features of the two composites are a direct consequence of the reaction pathways dictated by their respective iron precursors in the aqueous synthesis. The chemical speciation and solubility at the precursor stage fundamentally control the nucleation and growth kinetics, leading to either a heterogeneous mixture or a homogeneous solid solution.

The use of iron(II) sulfate with chloroplatinic acid creates a system prone to phase separation, whereby the rapid, unimpeded reduction of soluble $[PtCl_6]^{2-}$ ions leads to the fast nucleation of platinum-rich nanoparticles. Simultaneously, the introduction of OH^- ions causes the precipitation of iron(II) hydroxide ($Fe(OH)_2$), temporarily sequestering a portion of the Fe^{2+} and preventing it from participating in the co-reduction process (see Figure 5).

This kinetic decoupling results in a heterogeneous reaction sequence, beginning with the early-stage formation of a platinum-rich FCC solid solution and Pt nanocrystals. Fol-

lowing the depletion of the platinum precursor, a late-stage reduction of the remaining Fe^{2+} occurs, yielding ultra-fine metallic iron (XRNDPh) and localized, metastable iron-rich Fe-Pt phases. This temporal separation of reduction events inherently produces a heterogeneous composite. The resulting chemically unstable, oxidizable iron-rich domains are notoriously susceptible to oxidation, thereby accounting for the low chemical stability of Composite 1.

In contrast, the iron(III) ammonium sulfate precursor used for Composite 2 likely moderates these kinetics, favoring a more simultaneous reduction of both metal ions. The key mechanistic step is the precipitation of ammonium hexachloroplatinate, $(NH_4)_2[PtCl_6]$ (Ksp = 9×10^{-6} [32,33]), via an ion-exchange reaction. This precipitation first moderates the platinum release rate, thereby preventing the explosive nucleation of pure Pt clusters. Subsequently, the controlled, simultaneous availability of both metal precursors facilitates co-reduction and co-nucleation, preventing iron sequestration and leading to the observed homogeneous solid solution.

This kinetic synchronization favors the direct formation of a more compositionally uniform FCC solid solution and the emergence of a finely dispersed $Fe_{21}Pt_{79}$ ($L1_2$) intermetallic phase, even at low temperatures. The result is a homogeneous nanocomposite precursor with an iron content close to the target stoichiometry, engineered for superior thermal stability.

Ongoing experiments utilizing XPS (with Ar^+ etching) in couple with synchrotron radiation diffractometry are aimed at verifying these hypotheses through the analysis of spectral transformations during depth profiling.

5. Conclusions

This study demonstrates that the choice of iron precursor is a critical design parameter for controlling the architecture and phase composition of Fe-Pt nanocomposites synthesized via aqueous co-reduction. We have established a direct link between precursor chemistry and the resulting material's properties:

The use of iron(III) ammonium sulfate creates a reaction pathway that promotes homogeneity. The in-situ precipitation of $(NH_4)_2[PtCl_6]$ moderates platinum reduction kinetics, leading to the formation of a uniform, 5 nm FCC solid solution and facilitating the low-temperature formation of the $Fe_{21}Pt_{79}$ ($L1_2$) intermetallic phase. This results in a homogeneous and thermally stable nanocomposite that undergoes a controlled transformation upon annealing, with minimal grain growth.

In contrast, the use of iron(II) sulfate produces a heterogeneous and unstable composite. The rapid reduction of platinum leads to phase separation, yielding a mixture of Pt-rich nanocrystals, an iron-deficient solid solution, and chemically unstable, finely dispersed iron particles. This structure is prone to severe phase segregation and coarsening upon thermal treatment.

Therefore, the iron(III) ammonium sulfate precursor provides a superior and promising aqueous route for fabricating well-defined Fe-Pt nanocomposite precursors. These precursors are ideally suited for subsequent transformation into the high-performance $L1_0$-FePt phase, advancing the development of Fe-Pt composites for advanced magnetic applications.

Author Contributions: Conceptualization: A.N.P.; Methodology: A.N.P., V.M.P., and D.M.R.; Software: A.N.S. and D.M.R.; Formal analysis: N.S.Z., V.M.P. and N.S.A.; Investigation: N.S.Z., V.M.P., A.N.S., N.S.A. and D.M.R.; Data curation: N.S.Z. and V.M.P.; Writing—original draft: N.S.Z.; Writing—review & editing: A.N.P.; Supervision: A.N.P.; Project administration: A.N.P.; Funding acquisition: A.N.P. All authors have read and agreed to the published version of the manuscript.

Funding: This research was funded by the Russian Science Foundation, grant number 23-13-00356 (https://rscf.ru/project/23-13-00356/ (accessed on 1 November 2025)).

Data Availability Statement: The raw data supporting the conclusions of this article will be made available by the authors on request. The original contributions presented in this study are included in the article. Further inquiries can be directed to the corresponding author.

Acknowledgments: The authors acknowledge the following facilities and personnel for their contributions to this work: (1) The Center for Collective Use of the Federal Research Center for Coal and Coal Chemistry, SB RAS for elemental analysis (ICP-OES), X-ray diffraction (XRD), and in-situ high-temperature XRD measurements. (2) The Shared Research Facility of the Center of Synchrotron and Terahertz Radiation (Institute of Nuclear Physics, SB RAS, Novosibirsk) for precision synchrotron radiation diffraction experiments. (3) Kemerovo State University for conducting the transmission electron microscopy analysis.

Conflicts of Interest: The authors declare no conflicts of interest.

Abbreviations

The following abbreviations are used in this manuscript:

COD	Crystallography Open Database
CSR	Coherent Scattering Region
DFT	Density Functional Theory
EDX	Energy-Dispersive X-ray Spectroscopy
FCC	Face-Centered Cubic
HRTEM	High-Resolution Transmission Electron Microscopy
ICP–OES	Inductively Coupled Plasma–Optical Emission Spectrometry
PDF	Pair Distribution Function
SAED	Selected-Area Electron Diffraction
SR	Synchrotron Radiation
XPS	X-ray Photoelectron Spectroscopy
XRD	X-ray Diffraction
XRNDPh	X-ray Non-Detectable Phase

References

1. Gorbachev, E.A.; Kozlyakova, E.S.; Trusov, L.A.; Sleptsova, A.E.; Zykin, M.A.; Kazin, P.E. Design of Modern Magnetic Materials with Giant Coercivity. *Russ. Chem. Rev.* **2021**, *90*, 1287–1329. [CrossRef]
2. Skomski, R.; Sellmyer, D.J. Anisotropy of Rare-Earth Magnets. *J. Rare Earths* **2009**, *27*, 675–679. [CrossRef]
3. Kuz'min, M.D.; Tishin, A.M. Theory of Crystal-Field Effects in 3d-4f Intermetallic Compounds. In *Handbook of Magnetic Materials*; Brück, E., Ed.; Elsevier: Amsterdam, The Netherlands, 2007; Volume 17, pp. 149–233. [CrossRef]
4. Klemmer, T.; Hoydick, D.; Okumura, H.; Zhang, B.; Soffa, W.A. Magnetic Hardening and Coercivity Mechanisms in L10 Ordered FePd Ferromagnets. *Scr. Metall. Mater.* **1995**, *33*, 1793–1805. [CrossRef]
5. Chrobak, A. High and Ultra-High Coercive Materials in Spring-Exchange Systems—Review, Simulations and Perspective. *Materials* **2022**, *15*, 6506. [CrossRef]
6. Marciniak, J.; Werwiński, M. L10 FePt Thin Films with Tilted and In-Plane Magnetic Anisotropy: A First-Principles Study. *Phys. Rev. B* **2023**, *108*, 214406. [CrossRef]
7. Crisan, O.; Dan, I.; Palade, P.; Crisan, A.D.; Leca, A.; Pantelica, A. Magnetic Phase Coexistence and Hard–Soft Exchange Coupling in FePt Nanocomposite Magnets. *Nanomaterials* **2020**, *10*, 1618. [CrossRef]
8. Vishina, A.; Vekilova, O.Y.; Björkman, T.; Bergman, A.; Herper, H.C.; Eriksson, O. High-Throughput and Data-Mining Approach to Predict New Rare-Earth Free Permanent Magnets. *Phys. Rev. B* **2020**, *101*, 094407. [CrossRef]
9. Chen, X.; Zhang, S.; Li, C.; Liu, Z.; Sun, X.; Cheng, S.; Zakharov, D.N.; Hwang, S.; Zhu, Y.; Fang, J.; et al. Composition-Dependent Ordering Transformations in Pt–Fe Nanoalloys. *Proc. Natl. Acad. Sci. USA* **2022**, *119*, e2117899119. [CrossRef]
10. Gunakala, S.R.; Job, V.M.; Murthy, P.V.S.N.; Nagarani, P.; Seetharaman, H.; Chowdary, B.V. In-Silico Investigation of Intratumoural Magnetic Hyperthermia for Breast Cancer Therapy Using FePt or FeCrNbB Magnetic Nanoparticles. *Int. J. Therm. Sci.* **2023**, *92*, 108405. [CrossRef]

11. Chang, Z.X.; Li, C.H.; Chang, Y.C.; Huang, C.Y.F.; Chan, M.H.; Hsiao, M. Novel Monodisperse FePt Nanocomposites for T2-Weighted Magnetic Resonance Imaging: Biomedical Theranostics Applications. *Nanoscale Adv.* **2022**, *4*, 377–386. [CrossRef] [PubMed]
12. Hu, Z.; Wei, Q.; Zhang, H.; Tang, W.; Kou, Y.; Sun, Y.; Dai, Z.; Zheng, X. Advances in FePt-Involved Nano-System Design and Application for Bioeffect and Biosafety. *J. Mater. Chem. B* **2022**, *10*, 339–357. [CrossRef]
13. Bozuyuk, U.; Suadiye, E.; Aghakhani, A.; Dogan, N.O.; Lazovic, J.; Tiryaki, M.E.; Schneider, M.; Karacakol, A.C.; Demir, S.; Richter, G.; et al. High-Performance Magnetic FePt (L10) Surface Microrollers towards Medical Imaging-Guided Endovascular Delivery Applications. *Adv. Funct. Mater.* **2022**, *32*, 2109741. [CrossRef]
14. Choi, D.; Jang, I.; Lee, T.; Kang, Y.S.; Yoo, S.J. Overcoming Poisoning Issues in Hydrogen Fuel Cells with Face-Centered Tetragonal FePt Bimetallic Catalysts. *J. Mater. Sci. Technol.* **2025**, *207*, 308–316. [CrossRef]
15. Li, L.; Wang, Y.Z.; Wang, X.X.; Song, K.K.; Jian, X.D.; Qian, P.; Bai, Y.; Su, Y.J. Size and Stoichiometry Effect of FePt Bimetal Nanoparticle Catalyst for CO Oxidation: A DFT Study. *J. Phys. Chem. C* **2020**, *124*, 8706–8715. [CrossRef]
16. Sapkota, P.; Lim, S.; Aguey-Zinsou, K.F. Superior Performance of an Iron-Platinum/Vulcan Carbon Fuel Cell Catalyst. *Catalysts* **2022**, *12*, 1369. [CrossRef]
17. Zakharov, Y.A.; Popova, A.N.; Pugachev, V.M.; Zakharov, N.S.; Tikhonova, I.N.; Russakov, D.M.; Dodonov, V.G.; Yakubik, D.G.; Ivanova, N.V.; Sadykova, L.R. Morphology and Phase Compositions of FePt and CoPt Nanoparticles Enriched with Noble Metal. *Materials* **2023**, *16*, 7312. [CrossRef] [PubMed]
18. Zakharov, N.S.; Tikchonova, I.N.; Zakharov, Y.A.; Popova, A.N.; Pugachev, V.M.; Russakov, D.M. Study of the Pt-Rich Nanostructured FePt and CoPt Alloys: Oddities of Phase Composition. *Lett. Mater.* **2022**, *12*, 480–485. [CrossRef]
19. Pugachev, V.M.; Zakharov, Y.A.; Popova, A.N.; Russakov, D.M.; Zakharov, N.S. Phase Transformations of the Nanostructured Iron-Platinum System upon Heating. *J. Phys. Conf. Ser.* **2021**, *1749*, 012036. [CrossRef]
20. Wen, Z.; Wang, Y.; Wang, C.; Jiang, M.; Li, H.; Ren, Y.; Qin, G. Redetermination of the Fe–Pt Phase Diagram by Using Diffusion Couple Technique Combined with Key Alloys. *Int. J. Mater. Res.* **2022**, *113*, 428–439. [CrossRef]
21. Hao, Z.; Wei, L.; Wang, Y.; Kawazoe, Y.; Liang, X.; Umetsu, R.; Yodoshi, N.; Xia, W.; Zhang, Y.; Cao, C. Effect of Si Addition on the Magnetic Properties of FeNi-Based Alloys with L10 Phase through Annealing Amorphous Precursor. *J. Alloys Compd.* **2022**, *920*, 166029. [CrossRef]
22. Regulska, E.; Breczko, J.; Basa, A. Multifunctional $NiTiO_3$-decorated-rGO nanostructure for energy storage, electro- and photocatalytic applications. *Diam. Relat. Mater.* **2022**, *128*, 109310. [CrossRef]
23. Koryam, A.A.; El-Wakeel, S.T.; Radwan, E.K.; Darwish, E.S.; Abdel Fattah, A.M. One-Step Room-Temperature Synthesis of Bimetallic Nanoscale Zero-Valent FeCo by Hydrazine Reduction: Effect of Metal Salts and Application in Contaminated Water Treatment. *ACS Omega* **2022**, *7*, 34810–34823. [CrossRef]
24. Piminov, P.A.; Baranov, G.N.; Bogomyagkov, A.V.; Berkaev, D.E.; Borin, V.M.; Dorokhov, V.L.; Karnaev, S.E.; Kiselev, V.A.; Levichev, E.B.; Meshkov, O.I.; et al. Synchrotron Radiation Research and Application at VEPP-4. *Phys. Procedia* **2016**, *84*, 19–26. [CrossRef]
25. Lande, J.; Webb, S.M.; Mehta, A. Area Diffraction Machine. 2008. Available online: http://code.google.com/p/areadiffractionmachine (accessed on 18 November 2024).
26. *PDF-2 Database*; International Centre for Diffraction Data: Newtown Square, PA, USA, 2011.
27. Toby, B.H.; Von Dreele, R.B. GSAS-II: The Genesis of a Modern Open-Source All Purpose Crystallography Software Package. *J. Appl. Crystallogr.* **2013**, *46*, 544–549. [CrossRef]
28. Zakharov, Y.A.; Pugachev, V.M.; Korchuganova, K.A.; Ponomarchuk, Y.V.; Larichev, T.A. Analysis of Phase Composition and CSR Sizes in Non-Equilibrium Nanostructured Systems Fe-Co and Ni-Cu Using Diffraction Maxima Simulations in a Doublet Radiation. *J. Struct. Chem.* **2020**, *61*, 994–1000. [CrossRef]
29. Schneider, C.A.; Rasband, W.S.; Eliceiri, K.W. NIH Image to ImageJ: 25 Years of Image Analysis. *Nat. Methods* **2012**, *9*, 671–675. [CrossRef]
30. Momma, K.; Izumi, F. VESTA 3 for Three-Dimensional Visualization of Crystal, Volumetric and Morphology Data. *J. Appl. Crystallogr.* **2011**, *44*, 1272–1276. [CrossRef]
31. Persson, K.A.; Waldwick, B.; Lazic, P.; Ceder, G. Prediction of Solid-Aqueous Equilibria: Scheme to Combine First-Principles Calculations of Solids with Experimental Aqueous States. *Phys. Rev. B* **2012**, *85*, 235438. [CrossRef]
32. Patnaik, P. *Dean's Analytical Chemistry Handbook*, 2nd ed.; McGraw-Hill Education: New York, NY, USA, 2004.
33. Ginzburg, S.I. *Analytical Chemistry of Platinum Metals*; Israel Program for Scientific Translations: Jerusalem, Israel, 1975.

Disclaimer/Publisher's Note: The statements, opinions and data contained in all publications are solely those of the individual author(s) and contributor(s) and not of MDPI and/or the editor(s). MDPI and/or the editor(s) disclaim responsibility for any injury to people or property resulting from any ideas, methods, instructions or products referred to in the content.